Hindawi
International Journal of Intelligent Systems
Volume 2023, Article ID 1390828, 15 pages
https://doi.org/10.1155/2023/1390828

WILEY | Hindawi

Research Article

Real-Time Frequency Adaptive Tracking Control of the WPT System Based on Apparent Power Detection

Hongwei Feng,[1] **Yuanyuan Liu**,[2] **Conggui Huang**,[1] **Linbo Xie**,[3] **and Bin Qi**[1]

[1]*School of Control Technology, Wuxi Institute of Technology, Wuxi 214121, China*
[2]*Institute of Intelligent Manufacturing, Wuxi Vocational College of Science and Technology, Wuxi 214028, China*
[3]*Engineering Research Center of Internet of Things Applied Technology (School of IoT Engineering, Jiangnan University), Ministry of Education, Wuxi 214122, China*

Correspondence should be addressed to Yuanyuan Liu; lyyfhw@gmail.com

Received 25 September 2023; Revised 10 December 2023; Accepted 15 December 2023; Published 26 December 2023

Academic Editor: Yu-an Tan

Copyright © 2023 Hongwei Feng et al. This is an open access article distributed under the Creative Commons Attribution License, which permits unrestricted use, distribution, and reproduction in any medium, provided the original work is properly cited.

In wireless power transfer (WPT) systems, inverters are used to achieve high-frequency conversion of DC/AC, and their conversion efficiency and working frequency are key factors affecting the system's power transfer efficiency. In practical applications, many hardware issues, such as power transistor shutdown and loss, are the main reasons that affect the inverter conversion efficiency. On the other hand, the working frequency of WPT systems ranges from hundreds of kHz to a few MHz, and traditional voltage and current phasor estimation requires a very high sampling rate which is difficult to achieve. To overcome these limitations, this paper introduces a phase-shifting full bridge inverter using a zero-voltage switching (ZVS) soft switching technology to optimize the conversion efficiency of the inverter. Meanwhile, apparent power is introduced to detect the operating frequency and phase angle. Combined with an FPGA soft switching control strategy, this approach allows for the quick adjustment of the driving pulse of MOS transistors, as well as the voltage and current at the transmitting end, to a completely symmetrical state in real-time, effectively suppressing frequency offset and achieving efficient frequency tracking control and maximum efficiency tracking (MET) control of the WPT system. Through simulation and experiments, the ZVS soft switching technology has been achieved with the inverter control strategy, leading to improved conversion efficiency. The frequency offset that can be corrected can reach 0.1 Hz using the apparent power detection method, and the maximum transfer efficiency of the WPT system can reach 91%.

1. Introduction

With the rapid development of modern industry and technology, requirements for the convenience, intelligence, and safety of power supply are put forward. Wireless power transfer (WPT) technology has attracted widespread attention [1–3], and it has demonstrated application value in charging fields such as electric vehicles, consumer electronics, aerospace, and biomedical [4–7]. In WPT systems, changes in magnetic flux and current of the resonant coil are often caused by factors, such as environmental temperature, coil size, working conditions, and surface effects, resulting in differences between the theoretical resonant frequency and the actual resonant frequency, greatly reducing the system transfer efficiency. Therefore, frequency tracking is one of the key technologies to improve transfer efficiency by keeping the WPT system operating at resonant frequency.

To ensure that the WPT system operates at the resonant frequency point, there are three main control methods: coil topology optimization [8–10], dynamic compensation tuning [11–13], and frequency tracking. Compared to the other two methods, frequency tracking control is widely used in systems due to its easy implementation and fast response [14–21]. In [14], power allocation strategies are achieved targeted by adjusting the resonant frequency of the transmitting end to achieve stable output power that accurately counteracts load imbalance. However, there has been no in-depth research on the speed and accuracy in the frequency adjustment process. Reference [15] proposes an inverter control strategy based on pulse frequency modulation (PFM) and pulse width modulation (PWM) to achieve automatic tuning of the WPT system, enabling optimal efficiency tracking of the WPT system. In the research of self-tuning algorithms and phase detection methods, self-tuning and adaptive frequency tracking control (AFTC) of maximum transfer power for WPT systems through fuzzy PI algorithm is achieved in [16]. In [17], a variable frequency phase shift (VFPS) control strategy is proposed, calculating the instantaneous switching current of the power transistor to achieve zero-voltage switching (ZVS) operation with minimal frequency change. However, in practical applications, accurately collecting the instantaneous switching current can be challenging, which affects the control effect. Reference [18] proposes the frequency tracking algorithms to operate zero phase angle (ZPA) point for WPT systems based on second-order generalized integrator phase-locked loop (SOGI-FLL), reducing switching losses and improving the efficiency of inverters. Considering the manufacturing defects and aging issues of compensating capacitors in WPT systems, Reference [19] suggests applying the Sobol sensitivity method to rank the importance of the deviation of three capacitors on the transmission characteristics of the system. Additionally, a method to track the secondary resonance frequency to improve system performance is designed. A dual objective control strategy (DCS) is proposed in [20], adjusting the operating frequency of the high-frequency power amplifier and the duty cycle of the switching voltage to adapt to changes in distance between coils or output load changes, ensuring that the system can track the maximum power point under the optimal ZVS conditions. Reference [21] proposes an autonomous pulse frequency modulation scheme (APFM) for WPT battery charging; by extracting and processing the current signal on the primary side, the WPT system can adjust its output power by changing its duty cycle, achieving reliable ZVS.

Considering that many hardware issues, such as power transistor shutdown and loss in WPT systems, can lead to nonlinear drift of resonant frequency, the application of input voltage and current phasor estimation requires a high sampling rate when the inverter operating frequency reaches MHz, making it difficult to obtain the sampling rate in practical applications. This article proposes to use the input voltage and current of the WPT system to calculate the average values of active and reactive power, thereby obtaining the amplitude and phase of the input impedance. Then, in conjunction with the working mode of the inverter, an adaptive control strategy is introduced to quickly adjust the power MOS transistor driving pulse. This achieves efficient frequency tracking control, balances the current and voltage of the transmission circuit, and ensures that the system operates at maximum transfer efficiency in a resonant state.

The contributions of our work can be described as follows:

(1) Quantitative analysis was conducted on the source of the input ripple current of the inverter, providing a basis for further filtering out the low-frequency ripple current at the transmitting end of the WPT system and optimizing the frequency tracking algorithm

(2) A symmetrical PWM with ZVS soft switching technology was designed to achieve precise control of the inverter power transistor, thereby reducing switching losses and improving conversion efficiency

(3) An innovative method, combining FPGA to detect the operating frequency and phase angle of apparent power, was employed, and the MOS transistor driving pulse is quickly adjusted to achieve efficient frequency tracking and optimal power transmission

This paper is organized as follows. In Section 2, the overall circuit structure of the WPT system is introduced, and the topology structure and working mode of the inverter are analyzed. The real-time frequency adaptive tracking control method is presented in Section 3. Finally, experiments are presented in Section 4 to demonstrate the control performance of the real-time adaptive frequency tracking method. Section 5 provides the conclusions.

2. Frequency Analysis of the WPT System

2.1. Transfer Efficiency of the WPT System. A transmitting and receiving series (SS) resonant WPT system is taken into consideration for the study. In Figure 1, a typical SS topology is illustrated, where u_1 represents a high-frequency AC voltage source, i_1 and i_2 denote the high-frequency resonant currents of the transmitting and receiving loops, respectively. L_1, C_1 and L_2, C_2 are the inductors and capacitors of the transmitting and receiving loops, with R_1 and R_2 representing the internal resistances of L_1 and L_2, respectively, and R_L representing the load resistance of the resonant circuit. The two loops are magnetically linked with coupling coefficient $k = M/\sqrt{L_1 L_2}$, where M is the mutual inductance between the transmitting and receiving coils.

The following equations, derived from Kirchhoff's voltage law, can be obtained:

$$\begin{cases} \dot{U}_1 = Z_1 \dot{I}_1 - j\omega M \dot{I}_2, \\ 0 = Z_2 \dot{I}_2 - j\omega M \dot{I}_1. \end{cases} \tag{1}$$

Here, Z_1 and Z_2 are the equivalent impedances of transmitting and receiving ends, which satisfy the following equation:

$$\begin{cases} Z_1 = R_1 + j\left(\omega L_1 - \dfrac{1}{\omega C_1}\right), \\ Z_2 = R_2 + R_i + j\left(\omega L_2 - \dfrac{1}{\omega C_2}\right). \end{cases} \tag{2}$$

The transmitting and receiving coils have the same structure, that is, $L_1 = L_2 = L$, $R_1 = R_2 = R$, and $C_1 = C_2 = C$.

Therefore, by selecting appropriate parameters for L and C, the resonant frequency of the circuits on both sides can be determined, $f = 1/2\pi\sqrt{\mathrm{LC}}$.

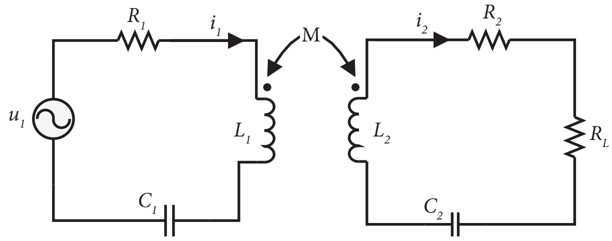

Figure 1: The identical circuit model of the WPT system.

From (1) and (2), the currents generated in the transmitting and receiving loops can be calculated as follows:

$$\begin{cases} \dot{I}_1 = \dfrac{Z_2 \dot{U}_1}{Z_1 Z_2 + \omega^2 M^2}, \\ \dot{I}_2 = \dfrac{j\omega M \dot{U}_1}{Z_1 Z_2 + \omega^2 M^2}, \end{cases} \tag{3}$$

where ω is the resonant angular frequency, satisfying $\omega = 2\pi f$. When resonance occurs, that is, $Z_1 = R$, $Z_2 = R + R_L$. The input power P_{in} and output power P_{out} of R_L can be expressed as follows:

$$\begin{cases} P_{\text{in}} = \dfrac{U_1^2 (R + R_L)}{R^2 + \text{RR}_L + \omega^2 M^2}, \\ P_{\text{out}} = \dfrac{\omega^2 M^2 U_1^2 R_L}{\left(R^2 + \text{RR}_L + \omega^2 M^2\right)^2}. \end{cases} \tag{4}$$

Here, U_1 is the RMS value of the input voltage. The system TE η can be derived from (4) as follows:

$$\eta = \frac{P_{\text{out}}}{P_{\text{in}}} = \frac{\omega^2 M^2 R_L}{(R + R_L)\left(R^2 + \text{RR}_L + \omega^2 M^2\right)}. \tag{5}$$

According to (5), when the positions of the transmitting and receiving coils in the WPT system are fixed, the system's transfer efficiency is mainly related to the resonant angular frequency ω. Once the resonant frequency deviates from its ideal value, the reactive power will increase and its transfer efficiency will be greatly reduced. The system's working frequency is closely related to the inverter's frequency. To mitigate the switching loss of the power transistor in the inverter and reduce the harmonic content of the voltage in the resonant network, this paper proposes a ZVS soft switching control strategy enabling the two bridge arms to work alternately at high and low frequencies while maintaining a balanced working state of the four power transistors in the inverter.

2.2. Analysis of the Inverter Topology. Figure 2 is a topological structure of the full bridge inverter. U_{in} is the power supply, the power tubes Q_a and Q_d form the leading bridge arm, and their driving voltages are u_{ga} and u_{gd}; Q_b and Q_c form a hysteresis bridge arm, with driving voltages of u_{gb} and u_{gc}; D_a~D_d are the freewheeling diode, $C_a \sim C_d$ are the resonant capacitor, L_f and C_f form the inverter side filtering circuit, and D_1~D_4 form the full wave rectifier bridge at the receiving end. u_1 is the voltage at the end of the RLC resonant network, which is a sinusoidal pulse width modulation (SPWM) wave controlled by a ZVS soft switching and synchronized with the modulation signal u_r.

Figure 3 shows the driving voltages u_{ga}, u_{gb}, u_{gc}, and u_{gd} of four MOS transistors, as well as the output signal diagrams of the H-bridge output terminal voltage u_{AB}. Here, u_c is the carrier signal, with amplitude U_c and frequency ω_c; u_r is a sine modulated signal with an amplitude of U_r and a working frequency of ω_r. The following is a characteristic analysis of the input current i_{in} of the inverter to determine the relevant parameters of the carrier and modulation waves.

Ignoring the switching dead zone of the full bridge inverter, the double Fourier series can be represented as the following switching function [22]:

$$f(\omega_c, \omega_{\text{r}}) = V \sin(\omega_r t) + \sum_{\text{m}=1}^{\infty} \frac{4}{m\pi} J_0\left(\frac{mV\pi}{2}\right) \sin\left(\frac{m\pi}{2}\right) \cos(m\omega_c t) + \sum_{m=1}^{\infty} \sum_{\text{n}=\pm1,\pm2\cdots}^{\infty} \frac{4}{m\pi} J_n\left(\frac{mV\pi}{2}\right) \sin\left(\frac{m+n}{2}\pi\right) \cdot \cos\left(m\omega_c t + n\omega_r t - \frac{n\pi}{2}\right). \tag{6}$$

Here, the regulation $V = U_r/U_c$; $m = 1, 2, 3, \ldots$, is the harmonic frequency of carrier signal u_c; $n = \pm1, \pm2, \pm3\cdots$, is the harmonic order of the modulated wave u_r; and $J_n(x)$ is the Bessel function [23].

The output voltage u_{AB} of the inverter can be expressed as a function of the DC voltage U_{in}:

$$u_{\text{AB}}(\omega t) = U_{\text{in}} \times f(\omega_c, \omega_t). \tag{7}$$

Correspondingly, the inverter outputs the filtered inductance current i_{Lf}, which can be expressed as follows:

$$i_{\text{Lf}}(\omega t) = \frac{u_{\text{AB}}(\omega t)}{Z(\omega)}, \tag{8}$$

where $Z(\omega)$ is the output impedance of the inverter at the corresponding angular frequency ω.

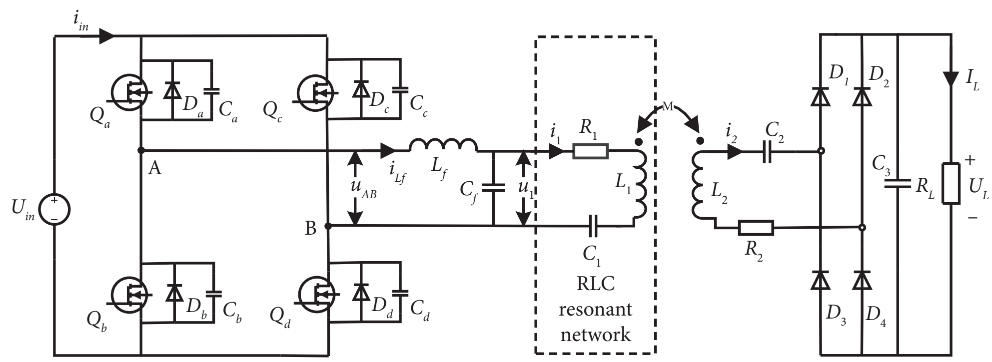

FIGURE 2: Topological structure of the full bridge inverter.

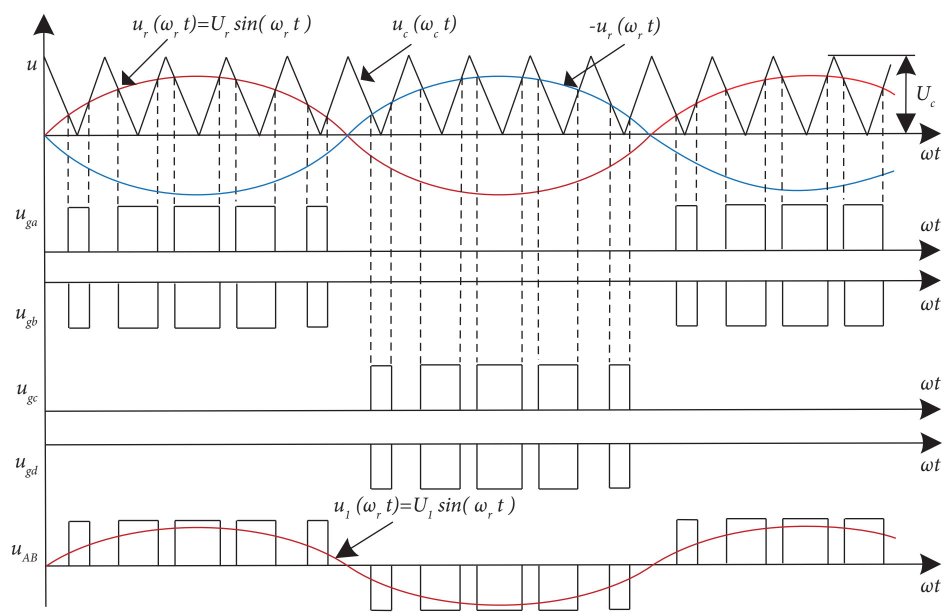

FIGURE 3: Power transistor drive signal and inverter output signal diagram.

Combining equations (6)–(8), the input current of the inverter can be expressed as follows:

$$
\begin{aligned}
i_{\text{in}}(\omega_c, \omega_r) &= i_{\text{Lf}}(\omega t) f(\omega_c, \omega_r) = \frac{u_{\text{AB}}(\omega t) f(\omega_c, \omega_r)}{Z(\omega)} = \text{U}_{\text{in}}\Bigg[M \sin(\omega_r t) \\
&\quad + \sum_{m=1}^{\infty} \sum_{n=\pm 1,\pm 2\cdots}^{\infty} \frac{4}{m\pi} J_n\left(\frac{mM\pi}{2}\right) \sin\left(\frac{m+n}{2}\pi\right) \times \cos\left(m\omega_c t + n\omega_r t - \frac{n\pi}{2}\right)\Bigg]\left[\frac{M}{Z(\omega_r)} \sin(y - \phi(Z(\omega_r)))\right. \\
&\quad + \sum_{m=1}^{\infty} \frac{4}{m\pi |Z(\text{m}\omega_c)|} J_0\left(\frac{mM\pi}{2}\right) \sin\left(\frac{m\pi}{2}\right) \times \cos(m\omega_c t - \phi(Z(\text{m}\omega_c))) + \sum_{m=1}^{\infty} \sum_{n=\pm 1,\pm 2\cdots}^{\infty} \frac{4}{m\pi |Z(\text{m}\omega_c + n\omega_r)|} \\
&\quad \left.\times J_n\left(\frac{mM\pi}{2}\right) \sin\left(\frac{m+n}{2}\pi\right) \times \cos\left(m\omega_c t + n\omega_r t - \frac{n\pi}{2} - \phi(Z(\text{m}\omega_c + n\omega_r))\right)\right].
\end{aligned}
\tag{9}
$$

In (9), $\varnothing(Z(\omega_x))$ is the impedance angle of the inverter output impedance at angular frequency ω_x.

To ignore the high-frequency admittance in the inverter, sufficient carrier wave ratio should be ensured to ensure that the high-frequency output impedances $Z(m\omega_c)$ and $Z(m\omega_c + n\omega_r)$ are much greater than the output impedance $Z(m\omega_c)$ of the RLC resonant network. Therefore, in this system, the frequency of selected carrier signal u_c is 1 MHz, and the frequency of modulation signal is 100 kHz. Therefore, the input current in (9) can be further simplified as follows:

$$i_{\text{in}}(\omega_c, \omega_r) = \frac{U_{\text{in}}V^2}{2|Z(\omega_r)|}\cos\left(\phi(Z(\omega_r)) - \frac{U_{\text{in}}V^2}{2|Z(\omega_r)|}\cos\left(2\omega_r - \phi(Z(\omega_r)) + \frac{2U_{\text{in}}V}{|Z(\omega_r)|}\sum_{m=1}^{\infty}\sum_{n=\pm1,\pm2\cdots}^{\infty}\frac{1}{m\pi}J_n\left(\frac{mV\pi}{2}\right)\right.\right.$$
$$\left.\left.\times\sin\left(\frac{m+n}{2}\pi\right)\left[\sin\left(m\omega_c + (n+1)\omega_r - \frac{n\pi}{2} - \phi(Z(\omega_r)) - \sin\left(m\omega_c + (n-1)\omega_r - \frac{n\pi}{2} + \phi(Z(\omega_r))\right]\right.\right.\right.\right. \tag{10}$$

According to (10), the input current of the full bridge inverter mainly comprises four components: DC component, carrier subharmonic, second harmonic, and carrier side frequency harmonic. It is evident that the inverter is equivalent to a nonlinear link in the WPT system, and there are also a large number of second harmonics in the input current, in addition to carrier harmonics and edge frequency harmonics. While high-frequency harmonics can be relatively easily filtered out by high-frequency capacitors, the second harmonic, with its lower frequency and higher content, poses challenges for hardware-based filtering. In the ZVS soft-switching process, special attention should be given to second harmonic filtering.

To fully achieve high-frequency inverter, each power transistor is connected in parallel with a capacitor, significantly reducing the stresses of du/dt and di/dt in the circuit, so that the power transistor can easily achieve zero voltage shutdown.

2.3. Analysis of the Working Mode of Inverters. Due to the symmetry of the positive and negative half cycles, the positive half cycle is taken for an example to analyze the six operating modes of the full bridge inverter in the WPT system under ZVS soft switching control. During the positive half cycle, power tubes Q_a and Q_b operate at high frequencies, with Q_d always on and Q_c always off. The equivalent circuit diagrams of the six working modes are shown in Figures 4(a)–4(f). u_{ca} and u_{cb} represent the terminal voltages of capacitors C_a and C_b, respectively, and u_{Qa} and u_{Qb} represent the terminal voltages of power transistors Q_a and Q_b, respectively The theoretical working waveforms under each working mode are shown in Figure 5.

Mode 1 ($t_0 \sim t_1$): the inverter is in a steady state with Q_a and Q_d power transistors conducting, $U_{\text{Ca}} = 0$, $U_{\text{Cb}} = U_{\text{in}}$, and the current i_{Lf} on the inductor L_f increases under the action of DC voltage U_{in}. When i_{Lf} reaches the peak current i_p, i.e., at time t_1, Q_a is turned off, and the current in the RLC resonant network is i_{1-p}.

Mode 2 ($t_1 \sim t_2$): the power tube Q_a is turned off, and i_{Lf} is used to charge the bypass capacitor C_a, causing the voltage at both ends to rise rapidly and discharge C_b. Due to the very short time $t_1 \sim t_2$, i_{Lf} has not changed much and is approximately a constant current source. Until time t_2, the voltage at both ends of C_b drops to 0, and the antiparallel diode D_b conducts.

Mode 3 ($t_2 \sim t_3$): at time t_2, D_b naturally conducts, causing Q_b to open at zero voltage. The inductance current i_{Lf} is in a continuous flow state until time t_3, $i_{\text{Lf}} = 0$. In this modal process, to ensure that Q_b achieves ZVS, it is necessary to maintain a dead band time before Q_a is closed and Q_b is opened.

Mode 4 ($t_3 \sim t_4$): after the current i_{Lf} drops to 0 at time t_3, the inverter module enters a zero initial state energy storage state, and the current in Q_b increases from 0 in a positive direction, when Q_b is turned off at zero voltage, i_{Lf} increases in reverse to $i_{\text{Lf}} - i_p$ at time t_4, and this mode ends.

Mode 5 ($t_4 \sim t_5$): after Q_b is turned off, the bypass capacitor C_a is discharged and C_b is charged. The time $t_4 \sim t_5$ is also very short, and the negative current i_{Lf} remains basically unchanged. By time t_5, U_{Ca} drops to 0.

Mode 6 ($t_5 \sim t_6$): at time t_5, D_a naturally conducts, causing Q_a turn on at zero voltage. At this time, the negative current i_{Lf} gradually decreases to 0. The input voltage U_{in} returns to positive direction to provide energy storage of L_f. The system returns to mode 1, and the next mode cycle begins.

As an important part of the WPT system, the inverter seeks to identify an effective frequency tracking control algorithm by analyzing its workflow for one cycle, thereby reducing the losses of each section of the inverter and improving the transfer efficiency of the WPT system. The introduction of apparent power is employed to detect the operating frequency and phase angle, facilitating precise frequency tracking in the subsequent section.

3. Real-Time Adaptive Frequency Tracking Method

The block diagram of the real-time detection phase angle structure is illustrated in Figure 6. The input voltage u_1 and current i_1 are extracted, through the extraction module,

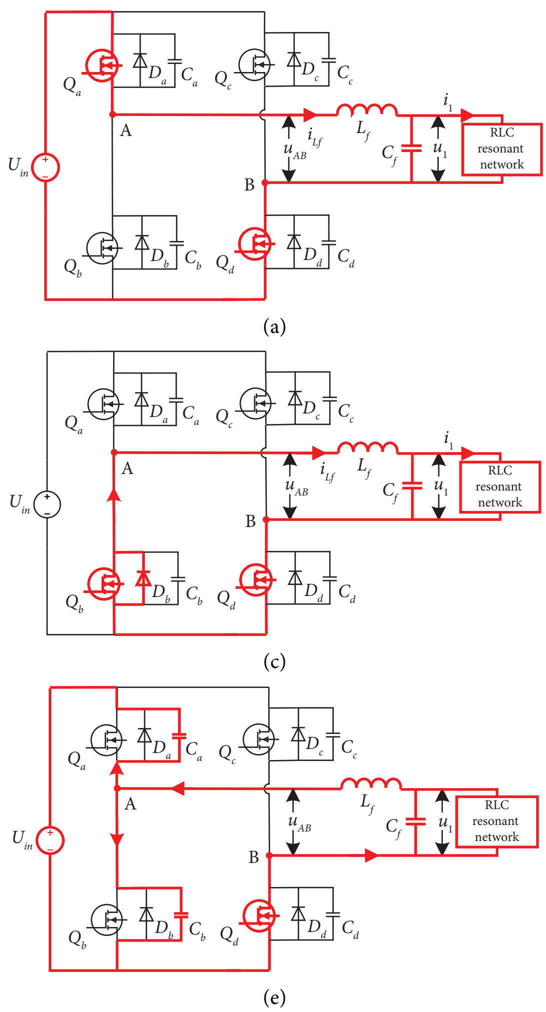

Figure 4: Main circuit diagram of the WPT system with constant output voltage control and MET control. (a) Mode 1. (b) Mode 2. (c) Mode 3. (d) Mode 4. (e) Mode 5. (f) Mode 6.

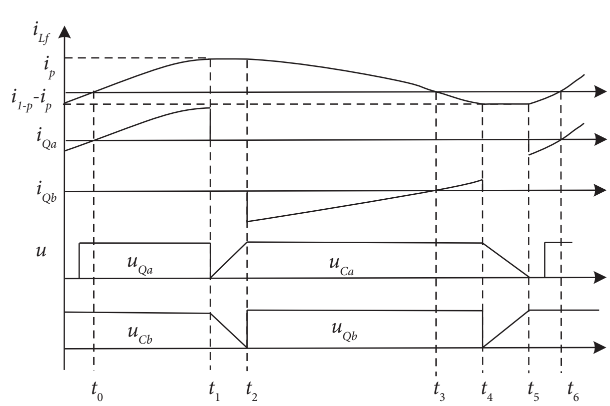

Figure 5: Theoretical working waveforms under various working modes.

which comprises active power P_1, reactive power Q_1, and the amplitude of input voltage $|U_1|$ of the WPT system. Combined with the FPGA frequency control word and phase accumulator, the MOS transistor driving pulse is rapidly adjusted through the ZVS soft switch control strategy to achieve efficient frequency tracking control and optimize the system's transfer efficiency.

3.1. Real Time Phase Angle Detection Method for Apparent Power. The input voltage u_1 and current i_1 are sinusoidal signals. The instantaneous active power can be calculated as follows:

$$p_1(t) = u_1(t) * i_1(t). \tag{11}$$

Considering $u_1(t), i_1(t)$ contains harmonic components, its expression can be written as follows:

$$u_1(t) = \sum_{k=1}^{n} U_{1k}\cos\left(\omega_k t + \beta_k\right), i_1(t) = \sum_{k=1}^{n} I_{1k}\cos\left(\omega_k t + \varphi_k\right). \tag{12}$$

In equation (12), U_{1k}, I_{1k} are the amplitudes of the first harmonic of $u_1(t), i_1(t)$, ω_k is the angular frequency, and β_k, φ_k are the initial phase. Then, $p_1(t)$ is represented as follows:

$$\begin{aligned} p_1(t) = {} & \frac{1}{2}\sum_{k=1}^{n} U_{1k}\sum_{j=1, j\neq k}^{n} I_{1j}\cos\left[\left(\omega_k + \omega_j\right)t + \left(\beta_k + \varphi_j\right)\right] + \frac{1}{2}\sum_{k=1}^{n} U_{1k}\sum_{j=1, j\neq k}^{n}\left\{I_{1j}\cos\left[\left(\omega_k - \omega_j\right)t\right.\right. \\ & \left.\left. + \left(\beta_k - \varphi_j\right)\right]\right\} + \frac{1}{2}\sum_{k=1}^{n} U_{1k}I_{1k}\cos\left[2\omega_k t + \left(\beta_k + \varphi_k\right)\right] + \frac{1}{2}\sum_{k=1}^{n} U_{1k}I_{1k}\cos\left(\beta_k - \varphi_k\right). \end{aligned} \tag{13}$$

The DC component of instantaneous power can be calculated as follows:

$$\overline{P} = \frac{1}{2}\sum_{k=1}^{n} U_{1k}I_{1k}\cos\left(\beta_k - \varphi_k\right). \tag{14}$$

The AC component of instantaneous power is represented as follows:

$$\begin{aligned} V = {} & \frac{1}{2}\sum_{k=1}^{n} U_{1k}\sum_{j=1, j\neq k}^{n} I_{1j}\cos\left[\left(\omega_k + \omega_j\right)t + \left(\beta_k + \varphi_j\right)\right] + \frac{1}{2}\sum_{k=1}^{n} U_{1k}\sum_{j=1, j\neq k}^{n}\left\{I_{1j}\cos\left[\left(\omega_k - \omega_j\right)t\right.\right. \\ & \left.\left. + \left(\beta_k - \varphi_j\right)\right]\right\} + \frac{1}{2}\sum_{k=1}^{n} U_{1k}I_{1k}\cos\left[2\omega_k t + \left(\beta_k + \varphi_k\right)\right]. \end{aligned} \tag{15}$$

Therefore, the active power has the following expression:

$$P_1(t) = \frac{1}{T}\int_0^T \left(\overline{P} + V\right)\mathrm{d}(t) = \frac{1}{T}\left(\int_0^T \overline{P}(t)\mathrm{d}t + \int_0^T V(t)\mathrm{d}t = \overline{P}\right). \tag{16}$$

From equation (16), it can be concluded that the DC component of instantaneous power is the active power. If an ideal low-pass filter is used to filter instantaneous power, active power can be obtained as follows:

$$P_1(t) \triangleq \frac{1}{T}\int_{t-T}^{T} p_1(t)\mathrm{d}(t) \cong \mathrm{LPF}\{p_1(t)\}. \tag{17}$$

In practical applications, an analog multiplier and LPF with a cut-off frequency of $2 * f/8$ are used, and the instantaneous reactive power $q_1(t)$ can be expressed as follows:

$$q_1(t) = u_1\left(t - \frac{T}{4}\right) * i_1(t). \tag{18}$$

At this point, a phase shifter is required. Therefore, $Q_1(t)$ can be calculated as follows:

$$Q_1(t) \triangleq \frac{1}{T}\int_{t-T}^{T} q_1(t)\mathrm{d}(t) \cong \mathrm{LPF}\{q_1(t)\}. \tag{19}$$

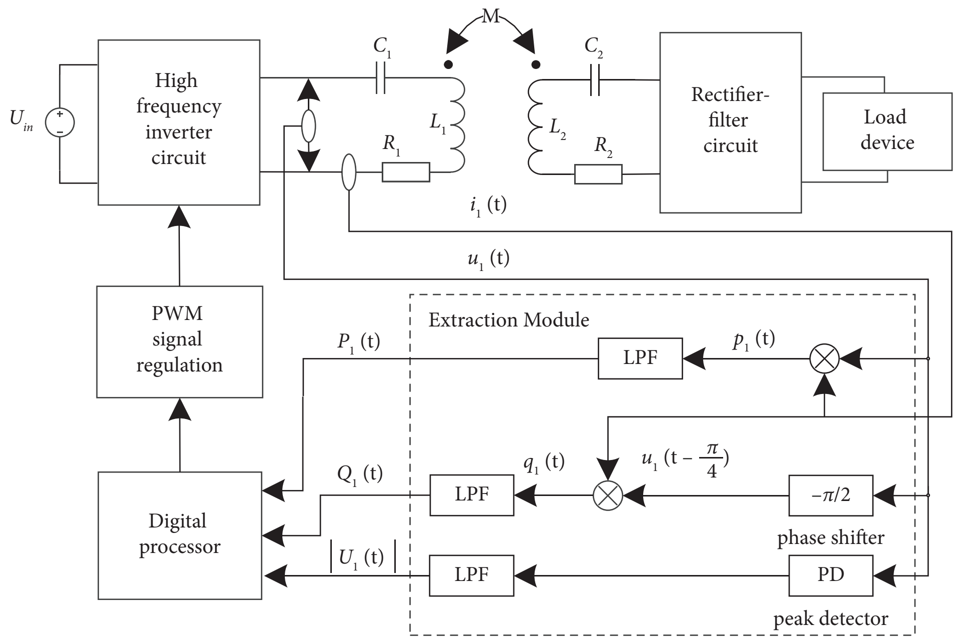

Figure 6: Real time detection phase angle structure diagram.

Finally, the amplitude of the input voltage U_1 of the WPT system can be obtained using a peak detector. The peak detector includes diodes, smooth RC, and LPF, which can be represented as follows:

$$|U_1| = \max\left\{\left|u_1\left(t'\right)\right|\right\}, \quad t - T \le t' \le t. \tag{20}$$

To calculate the impedance Z_1 of the input terminal, the following equation is used:

$$S_1 = U_1 I_1{}^* = U_1\left(\frac{U_1}{Z_1}\right)^* = \frac{|U_1|^2}{Z_1{}^*}, \tag{21}$$

$$Z_1 = \frac{|U_1|^2}{S_1^*} = \frac{|U_1|^2}{(P_1 - \mathrm{j}Q_1)}, \tag{22}$$

where $I_1{}^*, Z_1{}^*$ is the corresponding conjugate complex number of I_1, Z_1.

According to (22), it can be seen that only with active power P_1, reactive power Q_1, and the amplitude of input voltage $|U_1|$, the amplitude and phase angle of the input impedance Z_1 of the WPT system can be calculated as follows:

$$|Z_1| = \frac{|U_1|^2}{\sqrt{P_1{}^2 + Q_1{}^2}}, \tag{23}$$

$$\angle Z_1 = \Delta\theta = \arctan\left(\sqrt{\frac{Q_1}{P_1}}\right). \tag{24}$$

3.2. Adaptive Frequency Tracking Control Strategy. The frequency tracking processing program is determined as the highest priority, and FPGA is selected as the digital controller in this control strategy. The process of generating driving signals u_{ga}~u_{gd} is shown in Table 1, and the specific analysis is outlined as follows.

(1) Initialization of related parameters: according to the fixed frequency of the WPT system resonance circuit, set the number of timing clock pulses to N_0.
(2) Date collection and clock pulse number increment: the amplitude of active power P_1, reactive power Q_1, and input voltage $|U_1|$ are obtained by FPGA through sampling, and the phase difference $\angle Z_1$ of the input impedance Z_1 and its corresponding system clock pulse number ΔN are calculated.
(3) Comparison of the clock pulse number increment with the preset threshold δ: if it is greater than δ, proceed to step (4) for PWM adjustment. If not, consider that the system can automatically eliminate the difference without correction, and return to step (2). δ should be reasonably selected based on the primary side circuit of the phase-shifting full bridge transformer and the actual impedance phase difference.
(4) Adjust the square wave signal. Performing calculations based on $N = N_0 + \Delta N$, the square wave signal MB is adjusted with the same frequency and phase of $\angle Z_1 = 0$.
(5) FPGA generates an inverted signal MD based on the signal MB. According to signal MB, FPGA generates signal MA. First, determine the time $T_{\mathrm{MA}} = \mathrm{NDT_{clk}}$ for MA to maintain high level; second, determine the dead time $T_d = N_d T_{\mathrm{clk}}$, which is generally set to 80ns~100ns; when the falling edge of MB arrives, MA first maintains low

Table 1: Generating drive signal $u_{ga}\sim u_{gd}$ using FPGA.

(1)	Initialize parameters: N_0 Monitors: P_1, Q_1 and $\lvert U_1\rvert$
(2)	Calculate: Z_1 and $\angle Z_1$ using (22) and (24) Obtain the corresponding count value ΔN
(3)	If $\Delta N > \delta$, go to step (4); Else: go to step (2); End if
(4)	Calculate: $N = N_0 + \Delta N$ Adjust signal: MB
(5)	Generate inversion signal MD based on MB Calculate: T_{MA}, T_d Generate signal MA based on MB Generate signal MC based on MD
(6)	Generate driving signals: $u_{ga}\sim u_{gd}$

level for a time period T_d and then sets it to high level; MA maintains a high level for a time period T_{MA} and then sets it to a low level. In this process, the duty cycle during phase shift voltage regulation set to D, T_{clk} is the reference system clock, and N_d is the number of T_{clk} corresponding to the set dead time T_{MA}. The generation process of MC is the same as that of MA, and its reference signal is MD.

(6) The signals MA, MB, MC, and MD are, respectively, converted into $u_{ga}\sim u_{gd}$ through the driving circuit and supplied to the inverter power transistor $Q_a\sim Q_d$.

4. Simulation and Analysis of the Frequency Tracking System

4.1. Simulation Results and Analysis. A model of the WPT system was established based on Figure 1 for the proposed ZVS soft switching technology phase-shifting full bridge inverter and adaptive frequency real-time tracking control algorithm in the MATLAB/Simulink simulation environment. The relevant parameters of the simulation model are consistent with those of the experimental device, as shown in Table 2. Here, ω_c represents the carrier angular frequency, and D is the distance between the transmitting coil and the receiving coil.

4.1.1. The Simulation of ZVS Realization with Lagging Arm Q_C. The open critical waveform of ZVS realization with lagging arm Q_C can be observed in Figure 7, where u_{gc} is the driving waveform of Q_C, and U_{Qc} is the voltage waveform borne by Q_C. The dashed line 1 in Figure 7 indicates that before Q_C is opened, the pipe pressure drop U_{Qc} is 48 V. When Q_C is turned on, it is evident that U_{Qc} first drops to zero, and then the pulse voltage u_{gc} of the transistor rises, representing the process of zero voltage opening. It can be seen that before Q_C is turned off, the voltage dropping during Q_C conduction is approximately zero as indicated by the dashed line 2. When Q_C is turned off, Q_C receives the turning off pulse u_{gc} and returns to 48V, achieving zero voltage turning off.

4.1.2. Adaptive Frequency Tracking Simulation. In order to verify the adaptive ability of the frequency tracking algorithm when system parameters change, the capacitor C_1 in the resonant circuit jumps from 12.41 nF to 15.32 nF, and the resonance frequency of the system changes from 100 kHz to 90 kHz. Here are the waveforms of u_1 and i_1 in transmitting side with or without adaptive tracking control, which are shown in Figures 8 and 9.

Figure 8 illustrates the waveform without frequency tracking control. It can be seen that when frequency deviation occurs, in comparison to Figure 9, the amplitudes of u_1 and i_1 have a significant decrease, and a phase difference between u_1 and i_1 appears, which reduces the power factor of the transmitter. Figure 9 shows the waveform when adaptive frequency tracking control is added. The peaks of u_1 and i_1 are positive negative symmetric, ensuring that u_1 and i_1 are in the same frequency and phase, with no obvious DC component. The adopted adaptive frequency tracking scheme in this experiment effectively adjusts the waveform of the voltage and current at the transmitting end to be completely symmetrical along the axes. This suppression of the generation of reactive power contributes to an improvement in the power transfer efficiency of the WPT system.

4.2. Experiment Results and Analysis. To further validate the proposed adaptive frequency tracking control algorithm, a WPT system experimental platform was designed, and the devices are shown in Figure 10. The system parameters are shown in Table 2. The experimental schematic diagram of the WPT system is showed in Figure 11.

The schematic implementation is briefly analyzed as follows.

The obtaining of the peak of input voltage $\lvert U_1\rvert$: first, the instantaneous $u_1(t)$ is measured through a resistive voltage divider; the peak value of U_1 is measured using an analog peak detector (PD) consisting of a fast recovery diode (SS14) and a capacitor. Then, an analog low-pass filter (LPF) is used to remove the input voltage's ripples.

The measuring of current $i_1(t)$ using a current Hall sensor (ACS758LCB): $u_1(t)$ and $i_1(t)$ are multiplied using an analog multiplier (AD835), then the average value of active power $P_1(t)$ is extracted by an analog low-pass filter (LPF).

Similarly, an analog circuit which contains an operational amplifier (OPA2134PA) and an RC filter are used to generate a signal $u_1(t - T/4)$ by performing a phase shift of $-\pi/2$ on $u_1(t)$. Then, an analog multiplier (AD835) is used to multiply it with $i_1(t)$, and the average value of reactive power $Q_1(t)$ is extracted by using an analog LPF.

Combining with the adaptive tracking control strategy in Section 3.2, the collected data are analyzed by FPGA (EP1C3T144). The IR2110 module is selected as the driving circuit to achieve frequency tracking control of the system.

The experimental process and results analysis are presented as follows.

4.2.1. The Experiment of ZVS Realization with Lagging Arm Q_C. The voltage drop of the inverter MOS transistor is measured by a high-voltage probe, with a 10 times attenuation

Table 2: Parameters of wireless power transfer system.

Parameter	Value
U_{in}	48 V
R_1	0.482 Ω
R_2	0.481 Ω
C_1	12.41 nF
ω_c	6.28 M rad/s
C_2	12.42 nF
L_1	204.12 μH
L_2	203.96 μH
f_0	100 KHz
R_L	50 Ω

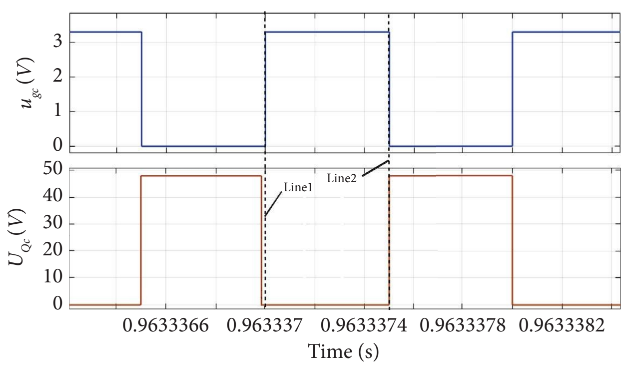

Figure 7: The open critical waveform of ZVS realization with lagging arm Q_C.

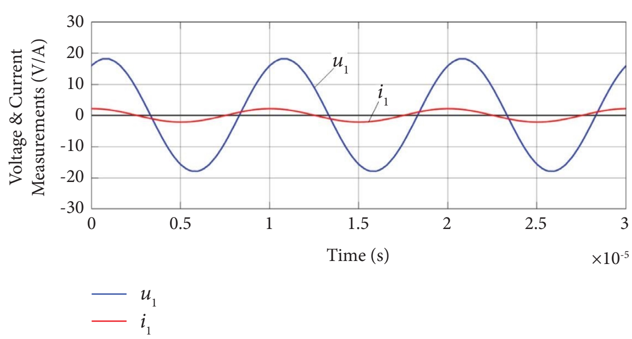

Figure 8: The waveform without adaptive frequency tracking algorithm.

factor. The critical waveform for opening the upper tube of the lagging arm Q_C is shown in Figure 12. It can be seen clearly that before Q_C is turned on, its pressure drop has basically decreased from 48 V to zero. The waveform of the shutdown process of Q_C is shown in Figure 13, demonstrating that when Q_C is turned off, the voltage drop of the tube increases slowly from zero, achieving zero voltage shutdown. Through simulation and experiments, it can be concluded that this design has achieved ZVS soft switching of the inverter, thereby improving the working efficiency of the inverter.

4.2.2. Experimental Verification of Adaptive Frequency Tracking. The experiment process is the same as the simulation, the capacitor C_1 in the system jumps from 12.41 nF

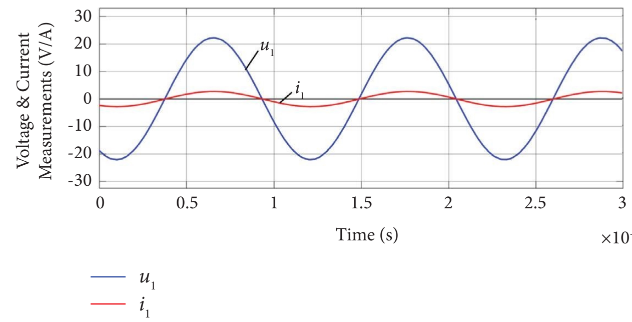

Figure 9: The waveform with adaptive frequency tracking algorithm.

to 15.32 nF, and the resonance frequency of the system changes from 100 kHz to 90 kHz. The waveforms of u_1 and i_1 in transmitting ends without and with adaptive frequency tracking control are recorded, as shown in Figures 14 and 15.

From Figures 14 and 15, it is evident that the introduction of an adaptive frequency tracking algorithm results in u_1 and i_1 exhibiting good positive and negative half-axis symmetry, with no obvious DC component, indicating stable system operation. The adaptive frequency tracking algorithm used in this experiment continuously adjusts the voltage and current at the transmitting end to be completely symmetrical, effectively suppressing the generation of frequency deviation and reducing system losses.

Then, the capacitor C_1 is adjusted from 15.32 nF to 12.41 nF, and the resonance frequency of the system changes from 90 kHz to 100 kHz. Figure 16 shows the tracking response curves between fuzzy PI adaptive control and the proposed method in this paper, when the inverter frequency is adjusted from 90 kHz to 100 kHz at $t = 0.5$ ms.

As shown in Figure 16, under the fuzzy PI adaptive tracking algorithm, the overshoot of the system is 8%, and the response time is about 1.3 ms. In contrast, under the tracking method proposed in this paper, the overshoot of the system is 6% and the response time is about 0.8 ms. Furthermore, it is confirmed that the proposed method can adjust the inverter drive signal in real-time based on the changing of $\angle Z_1$, when there is a significant change in the resonant frequency, ensuring that the system maintains a resonant state and exhibits fast dynamic response and good stability.

4.2.3. The Experimental Test of the System Transfer Efficiency. As previously mentioned, the maximum transfer power occurs at the resonant frequency, which is a function of the circuit resonant components (L_1, L_2, C_1, and C_2) and the coupling factor k. [16, 24] When the WPT system is determined, the system transfer efficiency is mainly related to the operating frequency and transmission distance, with a corresponding relationship between the resonant operating frequency and transmission distance of the system [25]. When the distance between the transmitting coil and the receiving coil changes, the coupling coefficient k will change, and the system transfer efficiency will also change. When the transmission distance closely aligns with the distance corresponding to the resonance frequency of the

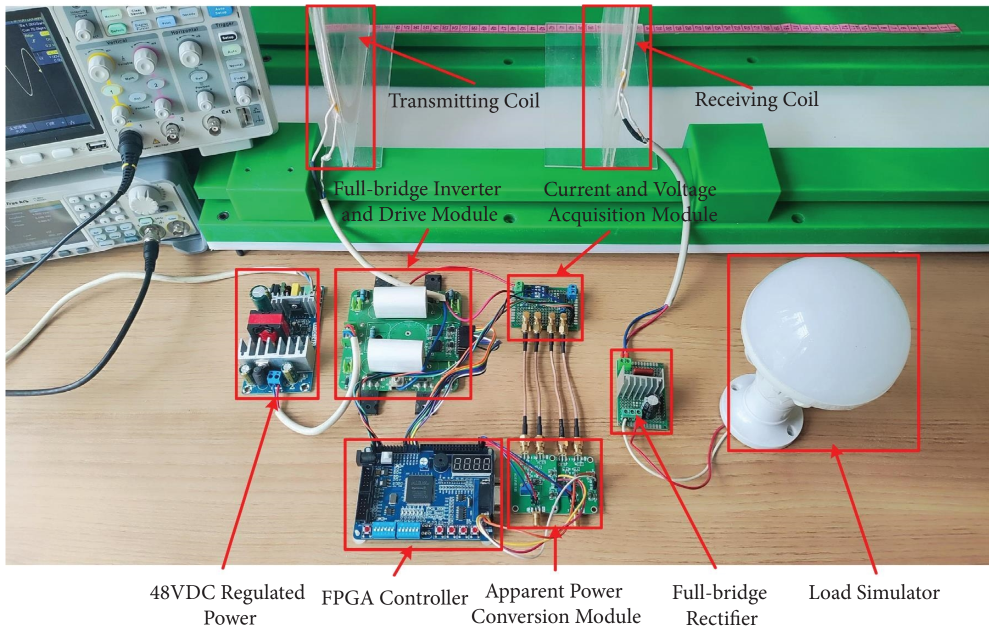

FIGURE 10: The experimental platform of the WPT system.

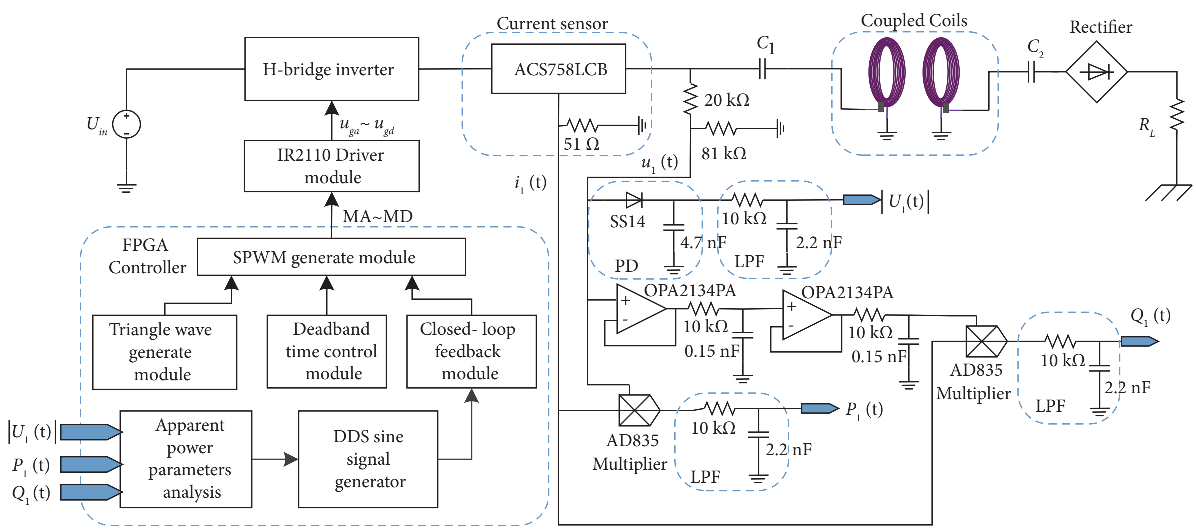

FIGURE 11: Schematic diagram of the proposed method.

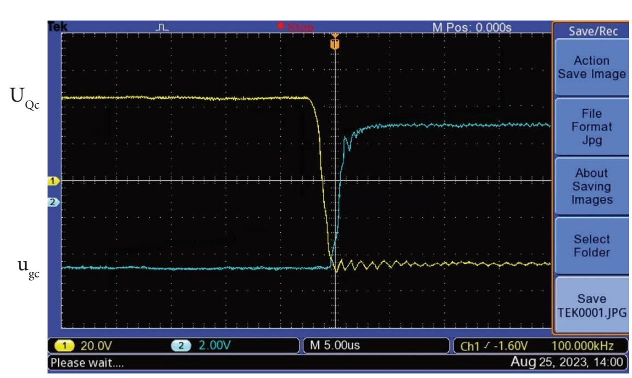

FIGURE 12: The opening waveform of lagging arm Q_c.

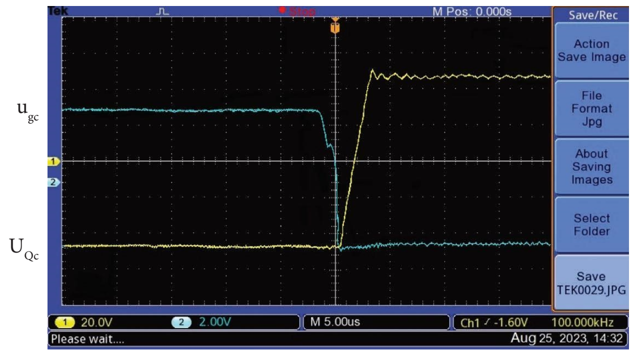

Figure 13: The shutdown waveform of lagging arm Q_c.

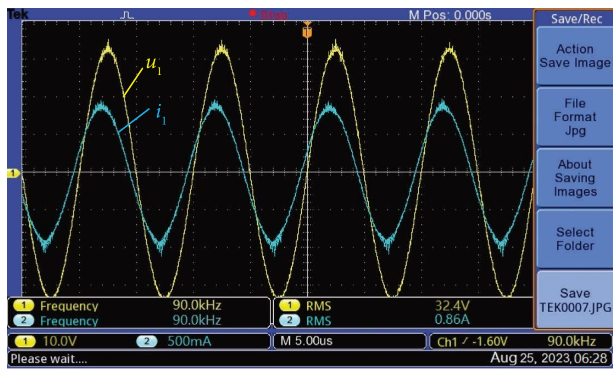

Figure 14: The waveform of u_1 and i_1 without adaptive control.

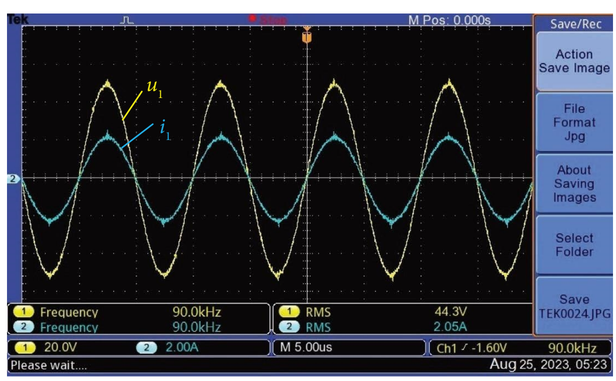

Figure 15: The waveform of u_1 and i_1 with adaptive control.

system, the transfer efficiency is the highest. By changing the distance between receiving and transmitting coils, the transfer efficiency of the WPT system with and without frequency tracking control is recorded in Figure 17.

The experimental results show that the adaptive frequency tracking control algorithm achieved by applying apparent power detection can adjust the working frequency of the inverter in real-time to ensure consistency with the system resonance frequency and adapt to any changes in coil distance. Among all the methods mentioned in this paper, not only does it exhibit robustness to coupling changes but it can also consistently provide global maximum transfer efficiency at any distance, showing excellent applicability.

The adjustment time, resonance frequency, efficiency improvement, system complexity, and maximum transfer efficiency with different frequency tracking control methods in [16–18, 20, 21, 26, 27] and this paper are shown in Table 3.

The similar operating frequencies, system power, and distance ranges have applied to the abovementioned control methods. Compared with the frequency control method in [16], significant advantages in adjusting time and transfer efficiency after frequency detuning have been obtained in this paper. Although the system adjustment time and transfer efficiency in [17, 20, 21] are relatively close to the methods proposed in this paper, but the system design complexity is relatively high and the application is difficult to achieve. The zero crossing

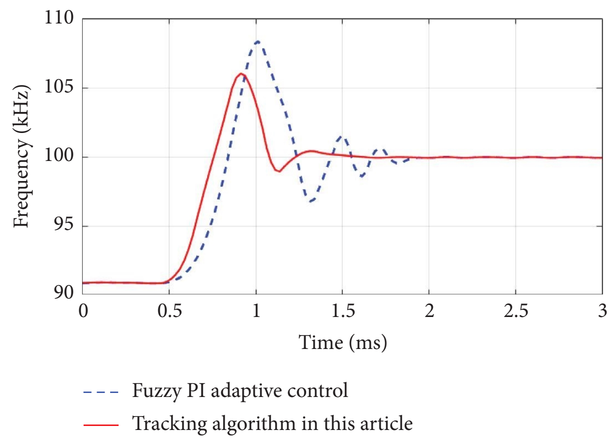

Figure 16: Tracking response curves of the frequency tracking algorithms.

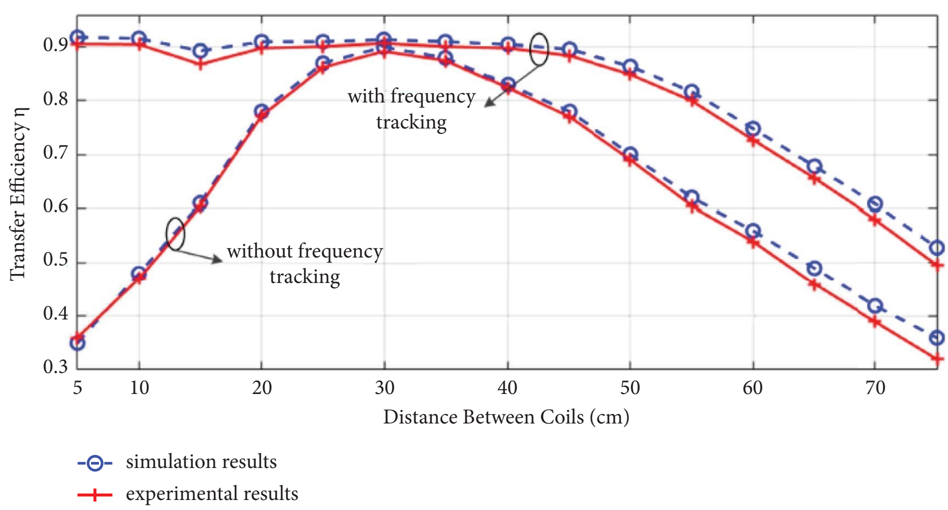

Figure 17: The transfer efficiency comparison curves.

Table 3: The summary of various indices for frequency tracking methods.

Reference	Method	Adjustment time (ms)	Resonant frequency (kHz)	Efficiency improvement (%)	Complexity	Maximum efficiency, η (%)
Zheng et al. [16]	AFTC	~300	85	3.6~4	Medium	86.9
Hu et al. [17]	VFPS	Not mentioned	85	~4	High	>91
Kim et al. [18]	PFM	2000	90	Not mentioned	High	~91
Nasr et al. [20]	DCS	~11	767	~8	High	88
Hua et al. [21]	APFM	Not mentioned	200	2.5	High	86.4
Matsuura et al. [26]	PFM (simulation)	Not mentioned	85	Not mentioned	High	85
Yang et al. [27]	PFM	~200	37~161.2	2.3	Medium	~70
This paper	AFTC	<1	100	4~5	Medium	91

comparison and phase detector are the main methods to achieve zero phase angle frequency tracking through inverter frequency modulation in [18, 26, 27], but it is difficult to handle multiple current zero crossing within the same cycle when dealing with over coupling conditions; as a result, there is no significant improvement in system's adjustment time and transfer efficiency. Compared with the mentioned methods, the proposed adaptive frequency tracking method in this paper has faster tracking speed and better correction ability in dealing with the problem of frequency detuning.

5. Conclusions

Adaptive frequency tracking of a full bridge phase-shifting inverter is achieved by real-time acquisition of apparent power and calculation of resonant circuit impedance angle in this paper, combined with ZVS soft switching technology. The proposed frequency tracking method can not only solve the problem of sampling rate limitation but also has a wide frequency adjustment range, fast tracking response, and high accuracy. The highest transfer efficiency of the WPT system can always be maintained through the theoretical and experimental results analysis.

Although this article has conducted in-depth and systematic research on the frequency tracking control key technologies in the WPT systems, there are still many issues that need further research due to the author's level and time, which can be summarized into the following two aspects:

(1) This paper adopts the fundamental harmonic analysis method when analyzing inverters and designing frequency control methods. In the situation that the quality factor of the resonant network is low, or output power changes significantly, the accuracy decreases with this analysis method. Therefore, methods based on time-domain analysis with the design of frequency tracking still need to be explored.

(2) Constant voltage output control has important application value in WPT systems. FPGA soft switching control strategy is combined to achieve efficient frequency tracking control in this paper, but the constant voltage output tracking control has not been considered. Therefore, an improved algorithm with adjustable PWM pulse duty cycle can be the next research object.

Data Availability

The data that support the findings of this study are available from the corresponding author upon reasonable request.

Conflicts of Interest

The authors declare that they have no conflicts of interest.

Acknowledgments

The authors would like to thank the support from the National Natural Science Foundation of the People's Republic of China under Grant no. 61873112 and Young and Middle-Aged Academic Leaders of the Qinglan Project in Jiangsu Province (2023), Jiangsu, China.

References

[1] Z. Zhang, H. Pang, A. Georgiadis, and C. Cecati, "Wireless power transfer-an overview," *IEEE Transactions on Industrial Electronics*, vol. 66, no. 2, pp. 1044–1058, 2019.

[2] M. Taghadosi and H. Kassiri, "A real-time-link-adaptive operation scheme for maximum energy storage efficiency in resonant CM wireless power receivers," *IEEE Transactions on Circuits and Systems I: Regular Papers*, vol. 68, no. 1, pp. 510–523, 2021.

[3] A. Trigui, M. Ali, S. Hached et al., "Generic wireless power transfer and data communication system based on a novel modulation technique," *IEEE Transactions on Circuits and Systems I: Regular Papers*, vol. 67, no. 11, pp. 3978–3990, 2020.

[4] C. Zhang, D. Lin, and S. Y. R. Hui, "Ball-joint wireless power transfer systems," *IEEE Transactions on Power Electronics*, vol. 33, no. 1, pp. 65–72, 2018.

[5] M. B. Lillholm, Y. Dou, X. Chen, and Z. Zhang, "Analysis and design of 10-MHz capacitive power transfer with multiple independent outputs for low-power portable devices," *IEEE Journal on Emerging and Selected Topics Topics Power Electron*, vol. 10, no. 1, pp. 149–159, 2022.

[6] A. Hossain, P. Darvish, S. Mekhilef, K. S. Tey, and C. W. Tong, "A new coil structure of dual transmitters and dual receivers with integrated decoupling coils for increasing power transfer and misalignment tolerance of wireless EV charging system," *IEEE Transactions on Industrial Electronics*, vol. 69, no. 8, pp. 7869–7878, 2022.

[7] X. Gao, W. Cao, Q. Yang et al., "Parameter optimization of control system design for uncertain wireless power transfer systems using modified genetic algorithm," *Centre for Applied Artificial Intelligence Transactions on Intelligence Technology*, vol. 7, no. 4, pp. 582–593, 2022.

[8] K. Song, Z. Li, Z. Du, G. Wei, and C. Zhu, "Design for constant output voltage and current controllability of primary side controlled wireless power transfer system," in *Proccedings of the 2017 IEEE PELS Workshop on Emerging Technologies: Wireless Power Transfer (WoW)*, pp. 1–6, Chongqing, China, May 2017.

[9] S. Djemoui, H. Allag, M. Chebout, H. R. E. H. Bouchekara, and E. H. Bouchekara, "Partial electrical equivalent circuits and finite difference methods coupling; application to eddy currents calculation for conductive and magnetic thin plates," *Progress in Electromagnetics Research C*, vol. 114, pp. 83–96, 2021.

[10] L. Aomar and H. Allag, "An Integro-Differential approach for Eddy currents computation in structures having heterogeneous Dimensions," *Progress in Electromagnetics Research M*, vol. 106, pp. 127–137, 2021.

[11] Y. Wang, Z. Yang, and F. Lin, "Design and implementation of wireless power transfer systems with improved capacitor error tolerance," *IEEE Transactions on Industrial Electronics*, vol. 69, no. 5, pp. 4707–4717, 2022.

[12] Y. Geng, Z. Yang, and F. Lin, "Design and control for catenary charged light rail vehicle based on wireless power transfer and hybrid energy storage system," *IEEE Transactions on Power Electronics*, vol. 35, no. 8, pp. 7894–7903, 2020.

[13] A. Ramezani, S. Farhangi, H. Iman-Eini, B. Farhangi, R. Rahimi, and G. R. Moradi, "Optimized LCC-series compensated resonant network for stationary wireless EV chargers," *IEEE Transactions on Industrial Electronics*, vol. 66, no. 4, pp. 2756–2765, 2019.

[14] X. Zhang, F. Liu, and T. Mei, "Multifrequency phase-shifted control for multiphase multiload MCR WPT system to achieve targeted power distribution and high Misalignment tolerance," *IEEE Transactions on Power Electronics*, vol. 36, no. 1, pp. 991–1003, 2021.

[15] A. Babaki, S. Vaez-Zadeh, A. Zakerian, and G. A. Covic, "Variable-frequency retuned WPT system for power transfer and efficiency improvement in dynamic EV charging with fixed voltage characteristic," *IEEE Transactions on Energy Conversion*, vol. 36, no. 3, pp. 2141–2151, 2021.

[16] Z. Zheng, N. Wang, and S. Ahmed, "Adaptive frequency tracking control with fuzzy PI compound controller for magnetically coupled resonant wireless power transfer," *International Journal of Fuzzy Systems*, vol. 23, no. 6, pp. 1890–1903, 2021.

[17] H. Hu, T. Cai, S. Duan, X. Zhang, J. Niu, and H. Feng, "An optimal variable frequency phase shift control strategy for ZVS operation within wide power range in IPT systems," *IEEE Transactions on Power Electronics*, vol. 35, no. 5, pp. 5517–5530, 2020.

[18] D. H. Kim, M. S. Kim, and H. J. Kim, "Frequency-tracking algorithm based on SOGI-FLL for wireless power transfer system to operate ZPA region," *Electronics*, vol. 9, no. 8, p. 1303, 2020.

[19] Y. Wang, Z. Yang, F. Lin, J. Dong, and P. Bauer, "Frequency tracking method and compensation parameters optimization to improve capacitor deviation tolerance of the wireless power transfer system," *IEEE Transactions on Industrial Electronics*, vol. 70, no. 12, pp. 12244–12253, 2023.

[20] F. Nasr, S. M. Madani, and M. Niroomand, "Dual-objective control strategy for maximum power and efficiency point tracking in wirelessly powered biomedical implanted devices," *Institution of Engineering and Technology Microwaves, Antennas and Propagation*, vol. 14, no. 1, pp. 36–44, 2020.

[21] Z. Hua, K. T. Chau, W. Liu, X. Tian, and H. Pang, "Autonomous pulse frequency modulation for wireless battery charging with zero-voltage switching," *IEEE Transactions on Industrial Electronics*, vol. 70, no. 9, pp. 8959–8969, 2023.

[22] S. Baldi, A. Papachristodoulou, and E. B. Kosmatopoulos, "Adaptive pulse width modulation design for power converters based on affine switched systems," *Nonlinear Analysis Hybrid Systems*, vol. 30, pp. 306–322, 2018.

[23] C. Uluisik and L. Sevgi, "A tutorial on Bessel functions and numerical evaluation of Bessel integrals," *IEEE Antennas and Propagation Magazine*, vol. 51, no. 6, pp. 222–233, 2009.

[24] X. Liu, X. Yuan, C. Xia, and X. Wu, "Analysis and utilization of the frequency splitting phenomenon in wireless power transfer systems," *IEEE Transactions on Power Electronics*, vol. 36, no. 4, pp. 3840–3851, 2021.

[25] M. Wang, J. Feng, Y. Shi, and M. Shen, "Demagnetization weakening and magnetic field concentration with ferrite core characterization for efficient wireless power transfer," *IEEE Transactions on Industrial Electronics*, vol. 66, no. 3, pp. 1–1851, 2018.

[26] K. Matsuura, D. Kobuchi, Y. Narusue, and H. Morikawa, "Communication-less receiver-side resonant frequency tuning for magnetically coupled wireless power transfer systems," *IEEE Access*, vol. 11, pp. 23544–23556, 2023.

[27] G. Yang and H. Liang, "Adaptive frequency measurement in magnetic resonance coupling based WPT system," *Measurement*, vol. 130, pp. 318–326, 2018.